Article:
Leong, Z., Huang, Y., Wróbel, J.S. et al. (2022) Pairwise dilatational strain as a parametric model describing potential secondary phase formation and high-angle grain misorientation in as-cast high-entropy alloys. Intermetallics, 144. 107462. ISSN: 0966-9795

https://doi.org/10.1016/j.intermet.2022.107462

Pairwise dilatational strain as a parametric model describing potential secondary phase formation and twinning propensity in as-cast high-entropy alloys

LEONG Zhaoyuan*[a], HUANG Yuhe[a,c], Jan S. WRÓBEL[b], GAO Junheng[a,d], Nicola MORLEY[a], and Russell GOODALL[a]

[a]Department of Materials Science & Engineering, Sir Robert Hadfield Building, Mappin St, Sheffield S1 3JD, UK

[b]Faculty of Materials Science and Engineering, Warsaw University of Technology, ul. Wołoska 141, 02-507 Warsaw, Poland

[c]Department of Materials Science and Engineering, Southern University of Science and Technology, No. 1088, Xueyuan Avenue, Nanshan District, Shenzhen, China

[d] Beijing Advanced Innovation Center for Materials Genome Engineering, University of Science and Technology Beijing, Beijing 100083, China

*Corresponding author: z.leong@sheffield.ac.uk

Abstract

Crystallographic strain in high-entropy alloys (HEAs) can affect not only structure stability, but also their mechanical properties. This is studied by comparing the effects of different alloying additions in CoCrFeNi-A_x (A: Mn, $V_{0.3}$, $Ti_{0.4}$, Pd_1, and $Pd_{1.5}$) FCC HEAs on their calculated dilatational strains. Dilatational strain values are found to be proportional to the EBSD population of misoriented microstructures at 53-60°. Larger magnitudes of the dilatational strain are exhibited by FCC-stabilising alloying additions. EBSD and TEM suggest increased twin presence for higher strain compositions. This means that HEAs can be designed to present higher ductility if dilatational strain can be maximised when structural stability can be maintained. These model-property relationships can be incorporated into metaheuristic objective functions as an alloy design strategy.

Keywords Intermetallics; high-entropy alloys; alloy design; SEM; microstructure; prediction; DFT

1. Introduction

LEONG Zhaoyuan - z.leong@sheffield.ac.uk. 2021

The ability of some near-equimolar alloys to form simple phases (FCC, BCC, and HCP) has catalysed research into compositions near the centre of phase diagrams [1–3]. These multicomponent (>4) alloys (MCAs), are termed as High-Entropy Alloys (HEAs) when demonstrating a single simple phase. Intermetallic-containing (or mixed phased) MCAs are referred to as Complex Concentrated Alloys (CCAs) [4] and can also be interesting for scientific study and technological applications.

How metals behave in response to energy is determined by thermodynamic principles, driven by energy minimisation. Sources of excess energy include grain boundaries and interphase boundary energies from secondary phase formation [5]. Due to high configurational entropy, the variation of local chemical ordering in HEAs plays a critical role in determining the energies of stacking faults and other critical defects, such as vacancies, interstitials, and twin boundaries [6]. Through compositional optimisation [7], the occurrence of deformation twinning and stress-induced phases can occur. These can be determined through first principle calculations for new alloys; *e.g.* Rice criterion can be used to determine relative ductility in HEAs [8,9]. Techniques like Density Functional Theory (DFT) can be time-consuming when applied for high-entropy compositions as convergence, parameter optimisation, pseudopotential selection *etc.* require optimisation. This is repeated for each composition stoichiometry that requires predictions. Parametric models trade off lower accuracy for reduced time, and can enhance the alloy design process. Their accuracy can be increased by refining modelling results through experimental verification and other relevant models or feeding them back into high-quality *ab-initio* DFT models to obtain more information.

Empirically, microstructural changes can be viewed as the variation of the boundary energy with orientation [5]; it can be considered to result from energy minimisation in a system under mechanical strain [5,10–12]. One pathway for the energy minimisation may be through the nucleation of secondary structures in the system (as discussed recently by Andreoli *et al.* [13]), through the formation of coherent or semi-coherent interfaces [14–16], noting that both interphase boundary and grain boundary energy will vary with the orientation of the boundary relative to the grain. Both the driving force for nucleation and grain boundary energies may be described through strain

fields [5,17], allowing analysis through this aspect. This is of interest as metastable HEAs may result in large strain fields when in the single phase [21] (although it should be noted that not all experiments on all materials agree that HEA lattices are highly strained [18]). HEA lattice strain has been used to predict structural stability by Toda-Caraballo and Rivera-Díaz-Del-Castillo [19]. Furthermore twining in multicomponent alloys may be amplified by the presence of affine shear strains [20,21]. This suggests that the strain in the system can be used to study the mechanical behaviour of HEA alloys.

We previously reported a parametric model to describe dilatational strain [22]. Since models not based on first-principles always have some level of inaccuracy from not fully considering electronic structure effects, they require robust comparison with experimental results to refine their accuracies. This way their intended use as complementary design tools alongside *ab-initio* or high-throughput experimental methods can be achieved. This paper will thus test the ability of the dilatational strain parametric model [22] as a design parameter to achieve targeted mechanical properties through a naïve determination of twinning likelihood in MCAs. MCA compositions are synthesised and in the spirit of heuristic modelling, the classification of their mechanical behaviours is explored using the dilatational strain model.

2. Methodology

The samples were prepared from pure elements by arc-melting in a low pressure, high-purity argon atmosphere. The sample was thoroughly re-melted at least three times to obtain an ingot which was then cast into a water-cooled copper mould to obtain as-cast cylindrical rods 3 mm in diameter and up to 40 mm in length.

The main phases and associated lattice parameters present in the as-cast condition were determined through x-ray diffraction on a STOE-STADI diffractometer using a Mo source to avoid luminescence effects from the alloying components.

Compression testing samples were sectioned into 6 mm with their ends ground and parallel following ASTM E9-89A which set the length-to-diameter ratio for cylindrical metallic bulk compression samples as 2.0 ± 0.05. Compression tests were then

performed at a nominal strain rate of $4 \times 10^{-5}s^{-1}$. Five samples were tested to failure, with another five interrupted tests performed to total true strains of 20% for electron backscatter diffraction (EBSD), and Transmission Electron Microscopy (TEM) analysis (to verify comparable microstructural behaviour between compositions).

Samples for backscatter electron (BSE) and EBSD imaging were mechanically polished down to a 3µm diamond suspension and twin-jet electropolished with a solution of 5% perchloric acid, 35% 2- butoxyethanol, and 60% methanol for 40s. Prior to EBSD observation, the samples were polished using a Gatan Precision Ion Polishing (PIPSII) system at 1kV, for 0.5h. BSE imaging and EBSD were performed using a field emission gun scanning electron microscope (FEI Inspect F50 FEG SEM) operating at 15kV for BSE imaging and 20kV for EBSD with a step size of 0.1µm for twinning and phase analysis. The EBSD data were analysed using HKL's CHANNEL5 post-processing software.

Density Functional Theory (DFT) calculations used in this study were carried out within the Vienna Ab-initio Simulation Package (VASP) using the Projector Augmented Wave (PAW) method and spin-polarized electronic structure scheme [23,24]. Exchange and correlation were treated in the Perdew–Burke–Ernzerhof generalized gradient approximation (PBE-GGA) [25]. PAW potentials were used without semi-core *p* electron contribution with 4, 5, 6, 7, 8, 9, 10, and 10 electrons treated as valence for Ti, V, Cr, Mn, Fe, Co, Ni and Pd, respectively. The plane wave cut-off energy applied in the calculations was 400 eV. Total energies were computed using Γ-centered Monkhorst-Pack mesh [26] of k-points in the Brillouin zone, with k-mesh spacing of 0.15 $Å^{-1}$, which corresponds to 6×6×6 Gamma-centred k-point meshes for a 2 x 2 x 2 supercell of FCC conventional unit cell containing 32 atoms. The total energy convergence criterion was set to 10^{-5} eV/cell. All structures were optimized allowing full relaxation of both ionic positions and cell shape with forces converged to below 10^{-2} eV A^{-1}. The disordered alloys were investigated by an application of special quasi-random structures (SQSs) [27] containing 32 atoms that were generated using a method based on a Monte Carlo simulated annealing loop [28] as implemented in the alloy theoretic automated toolkit (ATAT) package [29]. The elastic constants were computed by deforming an unstrained equilibrium structure and analysing the corresponding variation of the total energy as

a function of components of strain [30] whereas the anisotropy of Young's modulus defined as the ratio of standard deviation to average value of Young's modulus were calculated using the method proposed by Wrobel *et al.* in Ref. [31].

3. Results and Discussion

3.1 Alloy selection

CoCrFeNi-X compositions have been selected so that only the FCC structure is observed in all alloys, determined by referring to the literature and *via* comparison of semi-empirical parameters [3,32–34]. Since the parent composition CoCrFeNi has a FCC structure, the compositions have been carefully chosen so that the V and Ti additions are close to the FCC-secondary structure transition point [35]. This is so that any twin formation that occurs will follow the FCC twinning mode. We use VEC/ΔH biplots to select stoichiometric compositions that are near the borders of FCC stability (in the case of V and Ti additions) [35] in order to have alloys with high potential to break down forming twins or second phases, and to explore the differences between different alloying additions. The selected compositions are $Co_{25}Cr_{25}Fe_{25}Ni_{25}$, $Co_{22}Cr_{22}Fe_{22}Ni_{22}Ti_{13}$, $Co_{23}C3_{23}Fe_{23}Ni_{23}V_{07}$, $Co_{20}Cr_{20}Fe_{20}Ni_{20}Mn_{20}$, $Co_{20}Cr_{20}Fe_{20}Ni_{20}Pd_{20}$, and $Co_{18}Cr_{18}Fe_{18}Ni_{18}Pd_{27}$ respectively, which will be referred to as CCFN, CCFN-$Ti_{0.4}$, CCFN-$V_{0.3}$, CCFN-$Mn_{1.0}$, CCFN-$Pd_{1.0}$, and CCFN-$Pd_{1.5}$.

In a solid solution, the alloying elements (either interstitial or substitutional) will contribute to strain of the lattice. Since such strain in a hydrostatically stressed crystal (where the atoms may take any substitute on any lattice site) can be considered as a dilatational tensor, a dilatational strain model may be used to interpret the deformation behaviour of these alloys systems and phase stability [13,22]. The effects of the possible presence of strain within a HEA structure can be considered to be two-fold: 1) higher strain energy, ϕ_{strain} increases the barrier for dislocation movement and hence affects mechanical properties [36], and 2) heterogeneous nucleation of a secondary phase is only possible when the driving force for nucleation, δU is greater than the net increase in dilatational strain that results, ϕ_{strain} affecting the formation of complex phases [17]. The dilatational strain values are calculated following the method in [22] and its predictions are in agreement with the phase stability results

obtained through the VEC method. The significance of the values is discussed in later sections. To identify the phases in the synthesised compositions, XRD characterisation was performed.

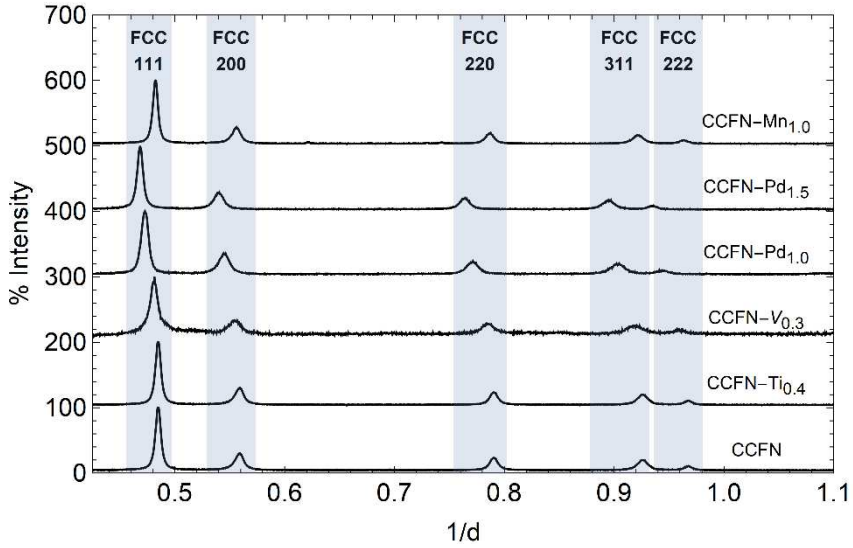

Figure 1. XRD patterns of FCC CCFN-A_x (A: Ti, V, Mn, and Pd). Each XRD pattern shows the (111), (200), (220), (222) peaks which are characteristic of the FCC structure, in good agreement with the predicted phase stability utilising typical semi-empirical models

XRD patterns of the as-cast compositions show that the majority phase in each case has the FCC structure; this is in good agreement with the reported results in literature [37–39]. It is observed that, in general, alloying additions to the CCFN structure expand the FCC lattice – its magnitude is dependent on the alloying additions used. V and Ti additions expand the FCC lattice minimally, as complex phase precipitation accompanies further increases in these elemental additions [40–42]. This explains the asymmetry of <111> peaks in CCFN-$Ti_{0.4}$, and CCFN-$V_{0.7}$, with a feature on the right shoulder of the peak, suggesting FCC phase segregation that may be a precursor to the formation of a secondary phase. This is in agreement with reports from the literature [35,40,41,43].

3.2 Compression behaviour

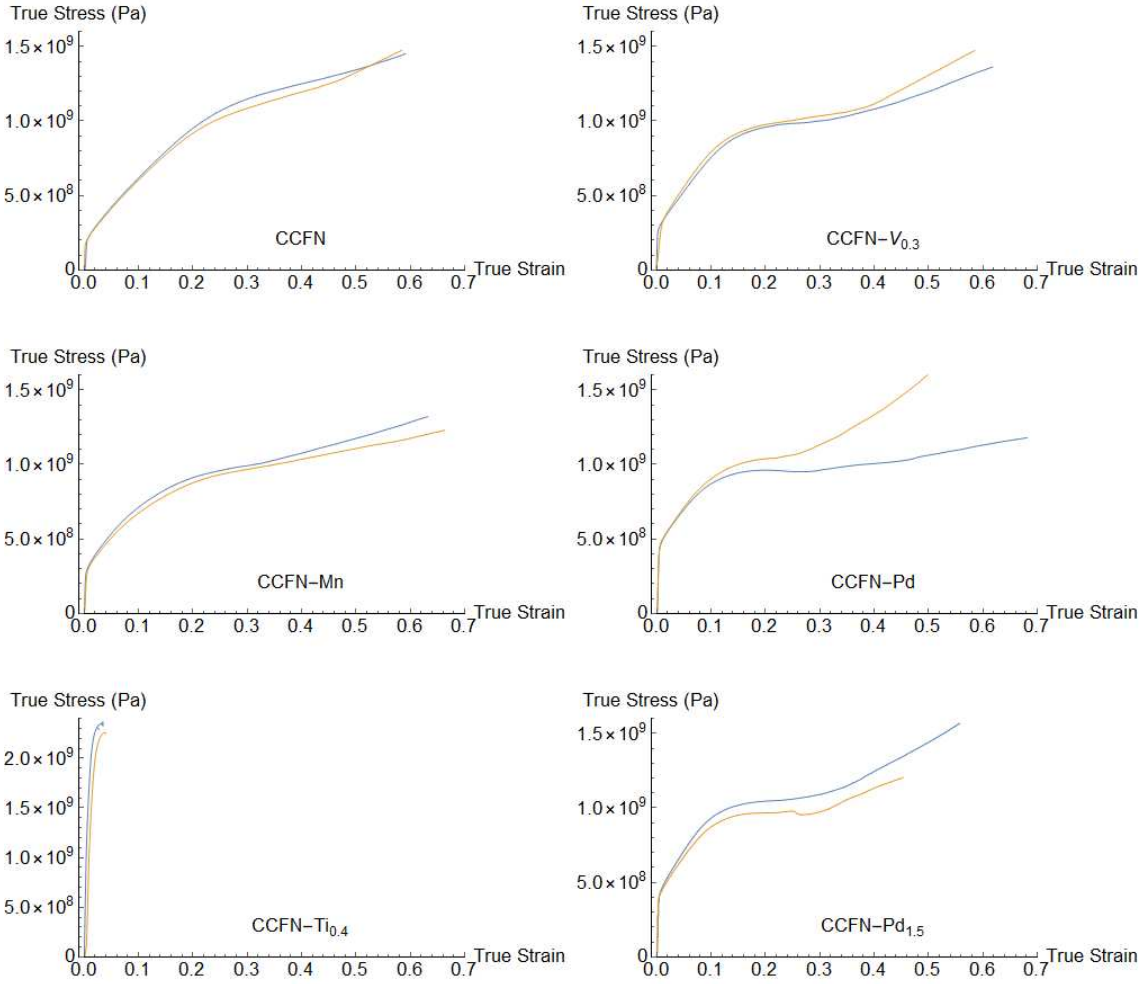

Figure 2. Compression test results of CCFN, CCFN-$Ti_{0.4}$, CCFN-$V_{0.3}$, CCFN-Mn and CCFN-Pd HEA compositions. The blue and orange lines correspond to each repeat measurement.

For each of the CCFN, CCFN-$Ti_{0.4}$, CCFN-$V_{0.3}$, CCFN-Mn, and CCFN-Pd compositions, two compression testing samples were prepared. The obtained results were corrected for the machine compliance and are presented the Appendix, showing that the repeats are in good agreement with each other. Errors are calculated to be <13% (calculations are available in the supporting documentation). The elastic modulus and 0.2% yield stress of the compositions were determined from the initial gradient of the compression test stress-strain curves and the intercept with the curve of a line with this gradient offset by 0.2% strain. The results are shown below in Table 1, presenting the average of the results obtained in each case.

Table 1. Summarised results of the compression tests showing 0.2% yield strength, elastic modulus.

Composition	0.2% Yield (MPa)	E_y Exp. (GPa)
CCFN	190	100
CCFN-$Ti_{0.4}$	1600	264
CCFN-$V_{0.3}$	290	160
CCFN-Mn	280	105
CCFN-Pd	240	150

Of the determined 0.2% yield strengths, CCFN-$Ti_{0.4}$ (1600MPa) is the highest, followed by CCFN-$V_{0.3}$ (290MPa), CCFN-Mn (280MPa), CCFN-Pd (240MPa), and CCFN (190MPa). The failure surface in CCFN-$Ti_{0.4}$ was observed to have brittle characteristics, while CCFN-$V_{0.3}$, CCFN-Mn, and CCFN-Pd undergo ductile deformation. It is noteworthy that the CCFN-$Ti_{0.4}$ composition possesses a negative enthalpy of mixing, outside the envelope commonly considered allowable for solid solution stability [32–34]. Thus, complex phase precipitation might be expected, despite the sample here displaying only peaks characteristic of the FCC phase from the XRD characterisation used (which may not record signal from phases present at very low volume fraction). This would explain the increased yield strength caused by precipitate strengthening. However, from Figure 2, the small Ti addition changes the elongation drastically, which suggests that some other effect other than precipitate formation may be a contributing factor. Previous work has shown that the electron density at the Wigner-Seitz Radius rapidly drops from 3.44×10^{29} m^{-3} (CCFN) to 2.96×10^{29} m^{-3} (CCFN-$Ti_{0.5}$) compared to 3.33×10^{29} m^{-3} (CCFN-$V_{0.3}$) and 3.22×10^{29} m^{-3} (CCFN-Pd) [44]. The lower value of CCFN-Ti is markedly different from those expected of a typical FCC HEA, and it may be expected that its deformation properties would be different as well.

Even between just the CCFN-$V_{0.3}$, CCFN-Mn, and CCFN-Pd compositions, which all show FCC structures in their as-cast state, there are appreciable differences in mechanical properties, indicating that the mechanical properties of these alloys are not determined simply by the phase displayed in as-cast states. There is also a significant increase of the 0.2% yield stress of all these samples above the value recorded for the

base CCFN alloy. While this difference may be associated with, for example, changes in the grain structure formed on casting, or the presence of second phases below the resolution limit of XRD, it would also be consistent with the increase in dilatational strain expected with the addition of a fifth element, due to the increased lattice misfit.

3.3 Deformation microstructures

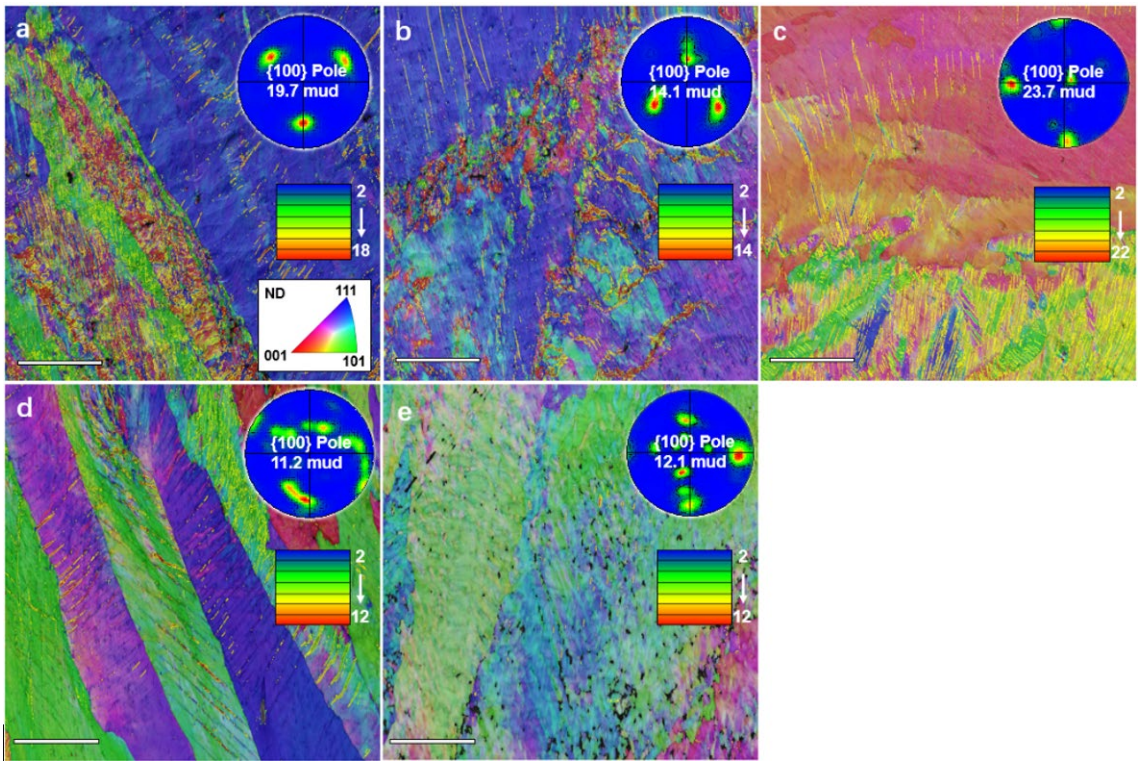

Figure 3. EBSD "IPF" images of deformed (from left) **(a)** CCFN-Mn; **(b)** CCFN-Pd; **(c)** CCFN-$Pd_{1.5}$; **(d)** CCFN-$V_{0.3}$; and **(e)** CCFN-$Ti_{0.4}$. For IPF colouring please refer to the inset. Insets correspond to (100) pole figures. Observation along ND was applied to IPF triangle of all samples. The EBSD (Pole figure) analysis is performed over a 300×300 µm area and captured for further analysis. Twining boundaries are highlighted with yellow lines. The 50 µm scale bar text is omitted for better viewability.

Previous results have shown that an increase in the shear strain may lead to enhanced plasticity and increased twin formation [45]. To study this behaviour in more detail, samples of each of the alloys under investigation were deformed to 20% compressive strain and were prepared for EBSD characterisation. Representative EBSD images of the compositions are shown in Fig. 3(a-e), where the twinning boundaries are

highlighted with yellow lines. The insets in Fig. 3(a–e) are (100) pole figures using data collected from IPF images of deformed samples. In Fig. 3(a-c), the pole figures of CCFN-Mn, CCFN-Pd and CCFN-$Pd_{1.5}$ exhibit obvious textures with a peak intensity of 19.7, 14.1 and 23.7 mud compared to the weaker deformed texture in CCFN-$V_{0.3}$ and CCFN-$Ti_{0.4}$ (Fig. 1(e)) with 11.2 and 12.1 mud peak intensity respectively. No similarity is observed in the texture component distribution in Fig. 4(a-e). However, taking the cumulative misorientation distribution as reference, the texture peak intensities share the same arrangement with the twinning volume fraction which is indicated by the grain boundaries close to the 60 degrees misorientation angle. The EBSD results, covering areas at least 300 × 300 µm were used to perform analysis of the misorientation over each boundary. The misorientation angles are shown for each alloy composition as cumulative frequency plots in Fig. 4.a

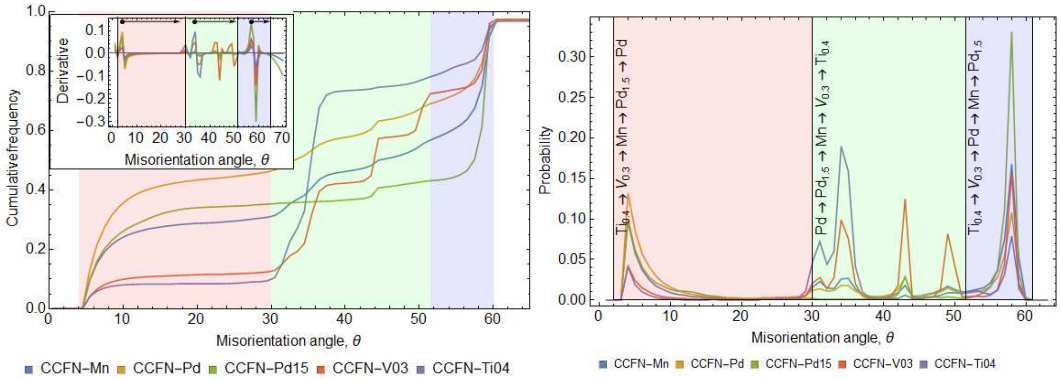

Figure 4. (a) Cumulative frequency plots of CCFN-A_x compositions with Zone 1 (red highlights), Zone 2 (green highlights), and Zone 3 (blue highlights) regions shown, **(inset)** The derivative of the cumulative frequency plot used to identify misorientation angle zones that are highlighted in red, green, and blue; and **(b)** Normalised cumulative frequency plots to determine the relative occupancy of each region for each alloy type. The relative occupancy is indicated next to the left border of each section.

Misorientation analysis of the results is necessary to decipher the underlying relationship. The cumulative frequency plots shown in Fig. 4a can be subdivided into different regions, arbitrarily demarcated, but selected to distinguish the locations of the major increments in cumulative frequency (shown by the derivative of the plots,

inset, Fig. 4a. *Zone 3* boundaries are often defined as having misorientation >53˚, and combined with the location of the increments, a cut-off was taken at 50˚, with all misorientations >50˚ being described in what follows as *Z3* (shown in blue in Fig. 4a). A significant increment in angle was seen at around 35˚, and another cut-off was taken here, with boundary misorientations 35˚< *x* < 50˚ being called *Zone-2, Z2* (MA shown as green). Finally, all misorientations below 35˚ are called in what follows *Zone 1, Z1* boundaries (LA, indicated by red).

In multicomponent alloys, due to the disparate nature of the alloying additions, there will be a solubility gap at low temperatures, as has been pointed out by Poletti *et al.* [46]. This leads to segregation within the solid solution at lower temperatures and therefore it is expected that coherency strains will increase until a precipitate of a new phase forms.

The formation of secondary phases due to enthalpy of mixing effects can be indirectly linked to the grain boundary misorientation (*e.g.* between non-miscible Cu and other elements [47]). It is known that high angle grain boundaries (typically >15 ˚) possess a higher driving force for segregation and fluctuations here are more like to evolve first into a critical nucleus for spinodal decomposition. Similarly, classical nucleation theory predicts that precipitation at high-angle boundaries have a larger contribution to the reduction of the interfacial energy. Referring back to the Z1 region in Figure 4, it is observed that the cumulative frequency does not change much past 15˚ until the 30˚ point which suggests that the Z1 demarcation presented here is comparable to low-angle grain boundaries. We would therefore expect the FCC stable containing alloying additions to have higher Z1 populations, and the complex-phase stabilising alloying additions to have a higher population in Z2.

Accordingly, in Fig. 4 it can be observed that the A: $V_{0.3}$ and $Ti_{0.4}$ compositions (which are Sigma and Laves phase stabilisers) possess the highest proportion of their misorientations in the MA range, and the lowest in Z1 (being the highest and lowest of all the compositions tested in these regions respectively). This is not surprising as the addition of even small amounts of solid-solution destabilising alloying additions is

sufficient to affect the electronic structure of the alloy system [44]. The reverse trend is observed for the A: $Mn_{1.0}$, $Pd_{1.0}$, and $Pd_{1.5}$ compositions.

In Fig. 4b it is observed that angles with the highest Z3 population also have the highest Z1 populations. This suggests that when the formation of a second phase of different structure (dominant in the medium misorientation angle zone) is available, for example to relieve stresses caused by dilatational strain effects, twinning (which would be seen at as very high or low misorientations) will be less prevalent, and *vice versa*.

3.4 Confirming twin presence *via* TEM

In the previous section it was seen that on the scale of a sample, the distribution across the low, medium and high range of the grain boundary misorientation angles may be correlated to the type of phases present. As the deformation processes here were carried out at room temperature, dynamic recrystallisation is not expected to occur, and thus the observed grain boundary misorientation around a misorientation angle of 50-60 degrees can be regarded as a feature of {111} FCC twinning. To confirm this, TEM was employed to determine the twinning relationship between the matrix and the various possible twining variants.

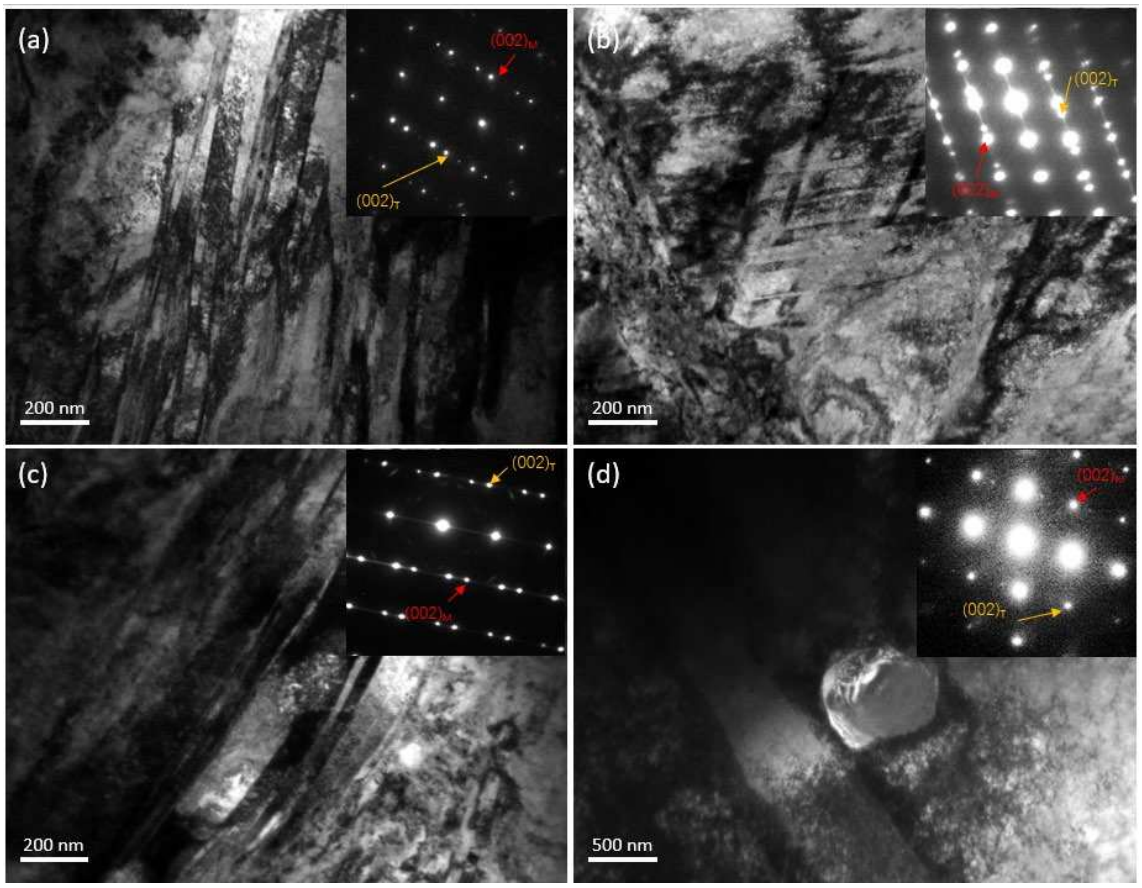

Figure 5. TEM images showing the variation of twin structure at the specimens cold-compressed to 20% strain with corresponding diffraction patterns, Beam direction is $[110]_{\gamma}$ for **(a)** CCFN-Mn; **(b)** CCFN-Pd; **(c)** CCFN-$V_{0.3}$; and **(d)** CCFN-$Ti_{0.4}$.

Figure 5 shows classical $\{111\}_{\gamma}$ twinning which was observed in all the studied compositions; CCFN-Mn, CCFN-$V_{0.3}$, CCFN-$Ti_{0.4}$, and CCFN-Pd. The twins observed in the micrographs are higher for the in CCFN-$V_{0.3}$ and CCFN-Pd and CCFN-Mn compositions in comparison to CCFN-$Ti_{0.4}$. These results are in good agreement to our EBSD result (*cf.* Figure 4b) where the cumulative frequency suggests that CCFN-$Ti_{0.4}$ possesses the lower proportion of twins as compared with the other compositions.

At this point we also would highlight that that the previous EBSD results indicate that the populations of grain boundaries in Z2 and Z3 (Fig. 4) follow opposite trends. The known complex phase-forming alloying additions (*A* = V and Ti) both exhibit a higher population of medium angle boundaries than the FCC-stable structures (*A* = Pd and Mn); the reverse is true for the high angle boundaries. It is noted that the CCFN-Mn

based compositions have been reported to show nanotwin formation [48]. These results, together with the TEM analyses, are in line with our hypothesis of the existence of competition between twin formation and phase precipitation in the deformation response of FCC HEAs.

3.6 Competition between the presence of twinning and incoherent grain boundaries

As solid solutions are stabilised below the critical temperature/metastability limit, a high lattice strain may no longer be required in the absence of spontaneous decomposition to balance the interfacial energies. It is thus expected that lattice strain decrease has a greater influence on CRSS for slip than twining [49]. This means that twinning may be preferred over slip as dilatational strain decreases.

Dilatational strain values can be calculated through evaluating the strain energy per atom in an unstrained matrix [5,17,22]:

$$\phi_{dil} = \frac{2\,G_m\,K_c}{3K_c+4G_m} \times \frac{(V_m-V_c)^2}{V_c} \qquad \text{(Eq. 1)}$$

where V_m and V_c are the volumes per molecule for the matrix and the cluster respectively, $E_{Y,m}$ and $E_{Y,c}$ are the Young's modulus for the matrix and the cluster respectively, and v_m and v_c are the Poisson's ratio for the matrix and the cluster respectively. Assuming a homogenous strain, the Voigt average is used to re-express the equation in terms of the elastic constants and the dilatational strain of the alloy system is evaluated by considering the sum of the paired dilatational strain values for each pair (denoted $\phi_{dil(m,c)}$ where m and c denote the matrix and cluster contribution as shown in Eq. 1) [22]:

$$\phi_{dil-pairwise} = \sum_{m,c=n}^{n=1,2,3\ldots} c_m\, c_c\ \phi_{dil(m,c)} \quad \text{(Eq. 2)}$$

where $C_{11,m}$, $C_{12,m}$, and $C_{44,m}$ are the elastic constants of the matrix and $C_{11,c}$, $C_{12,c}$, and $C_{44,c}$ are the elastic constants of the centre; c_m and c_c are the concentrations of the matrix and the cluster for each pair. Values of the elastic constants for the Voigt average are obtained from [50] and the elastic constants used are those of the elements in their unalloyed state. In the interest of brevity, all further mention of ϕ_{dil} in the text refers to

$\phi_{dil\text{-}pairwise}$ calculated from Eq. 2. The values for each alloy composition studied have been calculated from Eq. 2 and are of each EBSD group with their ϕ_{dil} values are shown below.

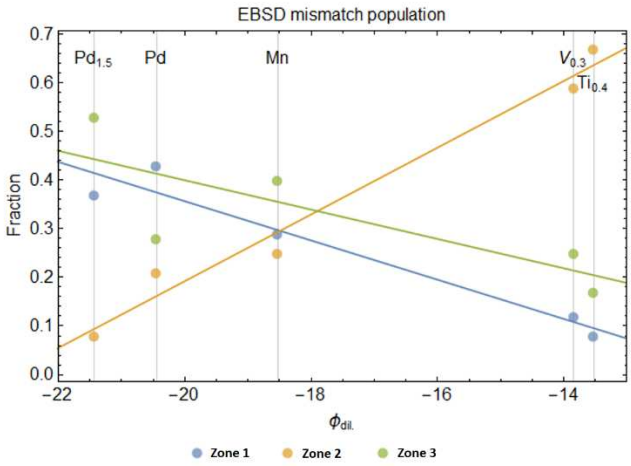

Figure 6. Plots of total Zone 1 (<30˚), Zone 2 (30-53˚), and Zone 3 mismatch (53-60˚) population plotted against ϕ_{dil} values, determined as described above. ϕ_{dil} values indicate the possible dilatational strain within the alloy system (as considered from the sum of the pair interactions), and are conjectured to lead to the formation of the microstructural defects behind processes such as twinning and/or slip that may enhance ductility during deformation processes.

From Fig. 6 it is observed that the gradients of the fitted lines of the Z1 and Z3 mismatch populations are of a different sign to the Z2 fit. As may be expected, the formation of similar phases for Z1 is linked to excess ϕ_{dil}. The Z2 trend lines where increased compositional segregation is expected, is inversely proportional to Z1. Two behaviour groups can be observed in Figure 6. Firstly, the FCC-stabilising alloying additions comprising of CCFN-Pd, CCFN-$Pd_{1.5}$ and CCFN-Mn have low misorientation fractions in Zone 2; the grain boundary misorientation fraction occupies Z1 and Z2. The reverse is true for the FCC-destabilising additions comprising of CCFN $V_{0.3}$ and CCFN-$Ti_{0.4}$ which has a higher fraction of grain boundary misorientation occupying Z2 in comparison to Z1 and Z3. It is known that strain can be used to predict HEA structural stability [19], which may explain the two different behaviours observed.

The excess ϕ_{dil} in the system may lead to the formation of microstructural features which will reduce the total energy of the system. It may be concluded empirically from

Figure 6 that a more negative ϕ_{dil} will be linked to a higher fraction of Zone 3 grain boundary misorientations, and therefore higher twins and ductility. This broadly agrees with first-principles calculations [8,9] to determine the Rice criterion for ductility of the CoCrFeNi HEA family, where Mn and Pd addition increases ductility, but Ti and V decrease ductility.

3.7 Driving force for nucleation of secondary phases

The driving force for nucleation of a secondary phase from a matrix is partly dependent on the strain energy of the system. The effective driving force for nucleation of a secondary phase can be related to the dilatational strain through [17]:

$$E_{eff} \propto -\mathrm{n}_c(\Delta\mu - \phi_{dil}) \qquad \text{Eq. 3}$$

where $\Delta\mu = kT\ Log(\frac{a}{a_e})$, $\mathrm{n_c}$ is the cluster size of the nucleate, and a and a_e are the actual and equilibrium activity of the former solid solution phase, and k and T are the Boltzmann constant and temperature, respectively. The above equation covers the decay of solids through nucleation of a new phase in a previous phase in which its components were dissolved and is valid for all instances where $a > a_e$. The activity, a is defined by:

$$\mu = \mu_0 + RT\ Log(a) \qquad \text{Eq. 4}$$

where μ and μ_0 are defined as the chemical potential of the system and chemical potential of the substitution, while R and T are the gas constant and the temperature, respectively. The Mulliken electronegativity (here denoted X) can be used to approximate the chemical potential at 0K [33,51]; using this and combining Eq. 3 and Eq. 4 gives the equation for a dilatationally strained system following the notation used previously for the matrix and the centre (respectively denoted m and c):

$$\Delta\mu = \frac{X_m - X_c}{c_m} \qquad \text{Eq. 5}$$

where c_m is the molar concentration of the matrix as the activity may be approximated as its molar concentration. E_{eff} values are in kJ/mol, and values of X for each element can be taken as the numerical mean of the first ionisation energy and the electron affinity. As the equation is applied to a multi-component system, we consider the total

pair interactions between the alloying elements to develop a figure of merit. Eq. 5 is therefore written as:

$$\Delta\mu = \sum_{n=i}^{i=1,2,3\ldots}\left(\frac{\left(\sum_{p=A}^{i=1,2,3\ldots} c_{p_n}\, c_{p_{n+1}}\, X_{p_n-p_{n+1}}\right)- X_{p_i}}{1-c_{p_i}}\right) \qquad \text{Eq. 6}$$

The values for $\Delta\mu$ are calculated for the compositions studied here and are shown as a biplot against the dilatational strain in Figure 7a.

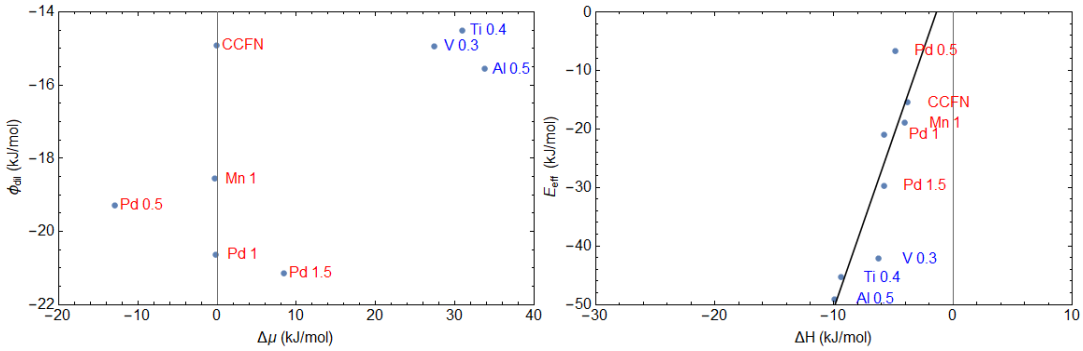

Figure 7. Analysis of the tendency for nucleation utilising a modified $\Delta\mu$ criterion by considering (a) A biplot of $\Delta\mu$ and ϕ_{dil} (both parameters contribute to the driving force for nucleation – the criterion $\Delta\mu > \phi_{dil}$ is required for this to happen); (b) The relationship between Miedema's ΔH [52,53] and E_{eff}. The alloys with experimental evidence indicating a tendency to form a secondary phase (ordered structures or intermetallic structures such as L12 and B2) are shown in blue, with the others in red.

$\Delta\mu$ values for the known secondary phase formers (A: $Ti_{0.4}$ and $V_{0.3}$,) are at least ≈3 times larger than the ones that remain in solid solution, resulting in pseudo E_{eff} values that are at least 1.5 times more negative than the other compositions (*cf.* Fig. 7 (b)). This analysis indicates that the effective supersaturation of the known secondary phase formers is higher (*i.e.* that there is a higher driving force for nucleation), resulting in an increased likelihood for the formation of secondary, complex phases in these alloys. It is useful to note that the CCFN-$Pd_{1.5}$ composition lies astride the centre of the calculated E_{eff} values; whilst many literature values have indicated that this composition possesses a single phase FCC structure [37,44,54], characterisation using neutron sources has indicated that the composition also possesses a secondary FCC

phase with similar lattice parameters and may experience compositional segregation [55,56].

It is observed that for compositions whose alloying additions only show the simple phase to be present, CCFN-$Mn_{1.0}$, CCFN-$Pd_{1.0}$, and CCFN-$Pd_{1.5}$, are observed to possess more negative ϕ_{dil} values as compared to CCFN-$V_{0.3}$, and CCFN-$Ti_{0.4}$ which adopt a majority complex phases structure at higher values of V, Ti, or Al addition [35,38,57]. This may be attributed to the fact that increased strain energy increases the energy associated with the compositional fluctuations within the solid solution and is known to reduce the driving force for nucleation from a strained matrix [17].

We would like to point out that the pair interaction approximation does not entirely reflect the changes at the electronic level, but provides a useful approximation of the behaviour seen. Fig. 7 (b) indicates a strong trend between values of E_{eff} and ΔH_{Mix}. It shows that the effective driving force for nucleation, E_{eff} decreases as ΔH_{Mix} decreases into more negative regions, towards regions of complex phase formation [32], and thus indicates that E_{eff} can give a comparative indication of the likelihood of nucleation of secondary phases for different compositions.

The reduced strain energy of the Ti and V containing compositions assessed here may be caused by phase transformation in the solid solutions with more negative ΔH values, due to increased ordering. The formation of complex phases would introduce interfaces, which would add to the total energy of the system. Assuming nucleation on grain boundaries and no change in strain energy, the effect of such changes on the total energy balance at the interface between the matrix and the secondary phase for incoherent alloying additions may be expressed as:

$$\gamma \approx \gamma_0 + \Delta G \qquad \text{(Eq. 9)}$$

where γ is the effective surface energy between the matrix/secondary phase, γ_0 is surface energy of grain boundaries before the nucleation of any secondary phase. ΔG is regarded as the minimum free energy required for the formation of the secondary phase. For the formation of a secondary phase the free energy must be negative, which therefore leads to a reduction in the energy of the system. Careful selection of

alloying elements with negative enthalpy of mixing values (which promote clustering) may thus provide a pathway for strain accommodation for compositions containing complex-phase stabilising elements, if the elemental additions can be picked so that a semi-ordered variant of the solid solution can be formed (*e.g.* FCC to L12, and BCC to B2) instead of a more ordered alternative structure.

At intermediate values of Miedema's enthalpy of mixing, $\Delta H > -7$, it is reported the formation of complex phases appears to be thwarted [32]. The exact mechanism of the simple phase stabilisation mechanism is unclear but may be partly attributed to the high value of mixing entropy and the low diffusivity of HEAs [58]. The inability for formation of a complex phase as a mechanism for strain energy reduction is reflected in the increasing strain energy seen for all FCC simple phases (CCFN-Mn and CCFN-Pd). Due to the increased strain energy present, systems with such characteristics may exhibit miscibility gaps in the solid phase; this may explain the instances of separation that have been observed for some compositions where multiple simple phases appear that are enriched with particular elemental combinations [14,39,56,59]. Miscibility gaps can also be attributed difference in atomic size radii (which is similar to the Hume-Rothery size effect), but can also be attributed to excess free energy and interactions of the electronic structure. Such metals may prefer to form stoichiometrically ordered phases (or intermetallics) where each element will have its own designated space in its lattice. Change in bond anisotropy (due to the specific positions that electronic orbitals may occupy as a result of hybridisation *etc.*) affects its elastic anisotropy (as compression and distortion of the electronic gas is affected) [60]. The addition of a single alloying element to a previously stable (as solid solution) four-component composition will then interact with each other for components. It may be inferred that the addition of alloying elements which show anisotropic elastic properties not only causes the precipitation of complex phases that are deleterious to mechanical properties [58] but also reduce the strain energies through rearrangement of the atoms into a semi-ordered structure that reduces the total free energy.

In general, the analysis shows that the increase in tendency to form secondary complex structures observed experimentally in the literature is correlated with a

decrease in the dilatational strain, calculated here considering the pair interactions between all alloying elements. This is in agreement with the hypothesis of this work where pathways for stress release may be through the nucleation of secondary structures in the system through the formation of coherent or semi-coherent phases [14–16].

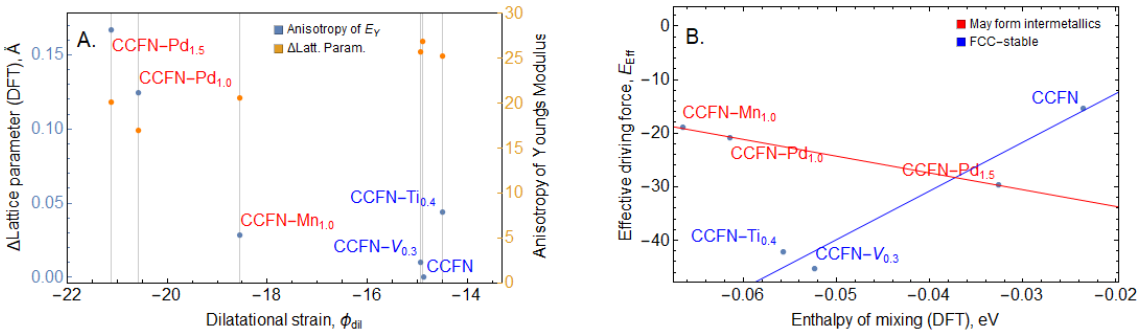

Figure 8. DFT calculations of **(a)** Biplots of DFT calculated changes in lattice parameter against the semi-empirical dilational strain and DFT-calculated elastic modulus anisotropy against dilatational stain; and **(b)** DFT-calculated mixing enthalpy against the effective semi-empirical driving force for nucleation.

In order to analyse the physical meaning of the dilatational strain terms calculated we perform DFT calculations on the compositions investigated here (finding the elastic modulus anisotropy, lattice parameters, and mixing enthalpy). The elastic modulus anistropy is defined as the standard deviation of Young's modulus divided by the average Young's modulus [31].

The results in Figure 8 (a) show the relationship between the *ab-initio* change in lattice parameter increases as the dilatational strain becomes more negative, which is expected due to the increase in lattice strain. Conversely, the calculated values of the anisotropy of the Young's modulus are noted to increase as dilatational strain becomes more positive. The elastic modulus can be defined as the second order derivative of the interaction potential with respect to equilibirum distance [61] which is to be expected as increased dilatational strain will affect the electron density due to lattice compression.

It has been pointed out that Miedema's enthalpy of mixing is incompatible with quantum principles [62]. Although these deviations are attributed to its capability to

predict phase stabilities in high entropy alloys [33], its accuracy limits its use as a tool in tying together physical phoenoemna with the electronic structure interactions. Figure 8 (b) therefore shows a similar plot to Figure 7 (b), but with enthalpy of mixing values calculated from DFT cluster-expansion calculations. These calculations show that the enthalpy of mixing becomes more proportionally negative with the effective driving force for nucleation for the intermetallic-stabilising compositions. Conversely, the gradient is reversed for the FCC-stabilising compositions, suggesting that some form of local segregation may take place resulting from the reduction in the effective driving force for nucleation. This is supported by high-resolution experimental results that show that HEAs may possess many similar structures with very small differences in lattice parameters which may be due to local compositional fluctuations [56,59], reflecting their metastable nature.

The non-linear nature of the dilatational strain that is dependent on the structure's propensity to remain in solid solution is illustrated in Figure 8 (b) in a plot of the driving force for nucleation calculated from Eq. 5. Here it is shown that the DFT mixing enthalpy has a positive gradient for the non-FCC stable phases (thus leading to precipitation), and has a negative gradient for the FCC-stable phases (thus leading to a build-up of energy within the system, which can act as a driving force for dislocation mechanisms). Thus the DFT results are in agreement with the hypothesis of this study.

These results in combination with the TEM analysis, and the comparison of the calculated nucleation driving forces with the known FCC-destabilising effect of Ti and V to CoCrFeNi strongly supports the hypothesis of the study. Together, they show that the dilatational strain can be used in combination with other semi-empirical structure-stability models as a strategy to further investigate and design interesting mechanical properties in high-entropy alloys.

Conclusions

In this work we have investigated the microstructural development of several strained (*via* compression) as-cast HEA compositions of CCFN-A (A: Mn, Pd, $Pd_{1.5}$, $Ti_{0.4}$, $V_{0.3}$) and indicates the suitability of dilatational strain as a heuristics model:

1. Experimental observations *via* EBSD (population at high-angle misorientation angles) suggest the formation of twins in CCFN-A (A: Mn, Pd, $Pd_{1.5}$, $Ti_{0.4}$, $V_{0.3}$). Twinning presence in all compositions was confirmed by TEM.
2. Dilatational strain (ϕ_{dil}) calculations were modified for multiple-component systems by evaluating the summed paired interactions of the alloying additions. Driving force for nucleation calculations ($\Delta\mu$) suggest that for Al, V, and Ti secondary structure formation is likely which agrees with the fact that they are known B2, Sigma and Laves phase formers. Compositional discrimination of the CCFN-$Ti_{0.3}$ and CCFN-$V_{0.4}$ compositions from CCFN-Mn, CCFN-Pd, and CCFN-$Pd_{1.5}$ is shown in the $\Delta\mu$ - ϕ_{dil} biplot, demonstrating the ability of the dilatational strain term in describing the effects of further alloying addition (secondary precipitation).
3. Population analysis of the boundary misorientations shows that the CCFN-Mn, CCFN-Pd, and CCFN-$Pd_{1.5}$ compositions possess a higher number of twins compared to the CCFN-$Ti_{0.3}$ and CCFN-$V_{0.4}$ compositions. Misorientation angles between 30-53˚ are present for the latter represent secondary phase formation although not present in the XRD analysis.
4. More negative dilatational strain values increase the EBSD misorientation angle fractions related to twining and coherent phase boundaries, and reduces the misorientation angle related to incoherent phase boundaries. Thus, the dilatational strain value can be calculated pre-synthesis, and may be used as a design parameter to indicate mechanical properties.
5. DFT results performed agree with the hypothesis of this study and the experimental results.

CRediT author statement

LEONG Zhaoyuan: Conceptualisation, Methodology, Software, Formal analysis, Investigation, Validation, Visualisation, Writing – Original Draft ; **HUANG Yuhe:** Validation, Formal analysis, Investigation, Visualisation, Writing – Original Draft;

Jan Wrobel: Methodology, Data curation, Validation, Formal Analysis, Writing – Review & Editing; **GAO Junheng:** Investigation; **Nicola MORLEY:** Supervision, Funding acquisition, Writing – Review & Editing; **Russell GOODALL:** Supervision, Funding acquisition, Writing – Review & Editing

Acknowledgements

ZL would like to acknowledge Professor Iain Todd for his invaluable discussions, and useful discussions with Juan Cornide, Peng Gong, and Jiawei Xi. This work was supported in part by the EU FP7/AccMet project [263206] and the Leverhulme Trust Research grant Scheme [RPG-2018-324]. RG would like to acknowledge a Fellowship supported by the Royal Academy of Engineering under the RAEng/Leverhulme Trust Senior Research Fellowships scheme [LTSRF1718_14_39]. JSW – The calculations were carried out with the support of the Interdisciplinary Centre for Mathematical and Computational Modelling (ICW), University of Warsaw, under grant No. GB79-6.

References

[1] E.J. Pickering, N.G. Jones, High-entropy alloys: a critical assessment of their founding principles and future prospects, Int. Mater. Rev. 61 (2016) 183–202. https://doi.org/10.1080/09506608.2016.1180020.

[2] J.W. Yeh, Recent progress in high—entropy alloys, Ann. Chim. - Sci. Mater. 31 (2006) 633–648.

[3] D.B. Miracle, O.N. Senkov, A critical review of high entropy alloys and related concepts, Acta Mater. 122 (2017) 448–511. https://doi.org/10.1016/j.actamat.2016.08.081.

[4] D. Miracle, J. Miller, O. Senkov, C. Woodward, M. Uchic, J. Tiley, Exploration and Development of High Entropy Alloys for Structural Applications, Entropy. 16 (2014) 494–525. https://doi.org/10.3390/e16010494.

[5] J.W. Christian, The theory of transformations in metals and alloys. Pt. 2: [...], 3. ed, Pergamon, Amsterdam, 2002.

[6] J. Ding, Q. Yu, M. Asta, R.O. Ritchie, Tunable stacking fault energies by tailoring local chemical order in CrCoNi medium-entropy alloys, Proc. Natl. Acad. Sci. 115 (2018) 8919–8924. https://doi.org/10.1073/pnas.1808660115.

[7] Z. Li, K.G. Pradeep, Y. Deng, D. Raabe, C.C. Tasan, Metastable high-entropy dual-phase alloys overcome the strength–ductility trade-off, Nature. 534 (2016) 227–230. https://doi.org/10.1038/nature17981.

[8] R. Mayahi, A theoretical investigation on deformation behavior and phase prediction of CoCrFeNi-based high entropy alloys, Mater. Today Commun. 24 (2020) 101025. https://doi.org/10.1016/j.mtcomm.2020.101025.

[9] M. Beyramali Kivy, M. Asle Zaeem, Generalized stacking fault energies, ductilities, and twinnabilities of CoCrFeNi-based face-centered cubic high entropy alloys, Scr. Mater. 139 (2017) 83–86. https://doi.org/10.1016/j.scriptamat.2017.06.014.

[10] K. Wang, J. Chen, X. Zhang, W. Zhu, Interactions between coherent twin boundaries and phase transition of iron under dynamic loading and unloading, J. Appl. Phys. 122 (2017) 105107. https://doi.org/10.1063/1.4997320.

[11] F. Dieter Fischer, T. Schaden, F. Appel, H. Clemens, Continuum Mechanics of Deformation Twinning – A Review, Multidiscip. Model. Mater. Struct. 2 (2006) 167–187. https://doi.org/10.1163/157361106776240789.

[12] N. Naeita, J. Takamura, Deformation twinning in silver-and copper-alloy crystals, Philos. Mag. 29 (1974) 1001–1028. https://doi.org/10.1080/14786437408226586.

[13] A.F. Andreoli, J. Orava, P.K. Liaw, H. Weber, M.F. de Oliveira, K. Nielsch, I. Kaban, The elastic-strain energy criterion of phase formation for complex concentrated alloys, Materialia. 5 (2019) 100222. https://doi.org/10.1016/j.mtla.2019.100222.

[14] E.J. Pickering, R. Munoz-Moreno, H.J. Stone, N.G. Jones, Precipitation in the equiatomic high-entropy alloy CrMnFeCoNi, Scr. Mater. 113 (2016).

[15] Z. Li, C.C. Tasan, H. Springer, B. Gault, D. Raabe, Interstitial atoms enable joint twinning and transformation induced plasticity in strong and ductile high-entropy alloys, Sci. Rep. 7 (2017) 40704. https://doi.org/10.1038/srep40704.

[16] I. Toda-Caraballo, P.E.J. Rivera-Díaz-del-Castillo, A criterion for the formation of high entropy alloys based on lattice distortion, Intermetallics. 71 (2016) 76–87. https://doi.org/10.1016/j.intermet.2015.12.011.

[17] D. Kashchiev, Nucleation basic theory with applications, Butterworth Heinemann, Oxford; Boston, 2000. http://www.engineeringvillage.com/controller/servlet/OpenURL?genre=book&isbn=9780750646826 (accessed February 20, 2016).

[18] L.R. Owen, N.G. Jones, Lattice distortions in high-entropy alloys, J. Mater. Res. 33 (2018) 2954–2969. https://doi.org/10.1557/jmr.2018.322.
[19] I. Toda-Caraballo, P.E.J. Rivera-Díaz-del-Castillo, Modelling solid solution hardening in high entropy alloys, Acta Mater. 85 (2015) 14–23. https://doi.org/10.1016/j.actamat.2014.11.014.
[20] S. Huang, H. Huang, W. Li, D. Kim, S. Lu, X. Li, E. Holmström, S.K. Kwon, L. Vitos, Twinning in metastable high-entropy alloys, Nat. Commun. 9 (2018). https://doi.org/10.1038/s41467-018-04780-x.
[21] B. Gludovatz, A. Hohenwarter, K.V.S. Thurston, H. Bei, Z. Wu, E.P. George, R.O. Ritchie, Exceptional damage-tolerance of a medium-entropy alloy CrCoNi at cryogenic temperatures, Nat. Commun. 7 (2016) 10602. https://doi.org/10.1038/ncomms10602.
[22] Z. Leong, N. Morley, R. Goodall, Dilatational strain biplots against enthalpy of mixing for predicting high-entropy alloys and complex concentrated alloys phase stability, Mater. Chem. Phys. 262 (2021) 124241. https://doi.org/10.1016/j.matchemphys.2021.124241.
[23] G. Kresse, J. Furthmüller, Efficiency of ab-initio total energy calculations for metals and semiconductors using a plane-wave basis set, Comput. Mater. Sci. 6 (1996).
[24] G. Kresse, J. Furthmüller, Efficient iterative schemes for ab initio total-energy calculations using a plane-wave basis set, Phys. Rev. B Condens. Matter. 54 (1996).
[25] J.P. Perdew, K. Burke, M. Ernzerhof, Generalized Gradient Approximation Made Simple, Phys. Rev. Lett. 77 (1996) 3865–3868. https://doi.org/10.1103/PhysRevLett.77.3865.
[26] H.J. Monkhorst, J.D. Pack, Special points for Brillouin-zone integrations, Phys. Rev. B. 13 (1976) 5188–5192. https://doi.org/10.1103/PhysRevB.13.5188.
[27] A. Zunger, S. Wei, L. Ferreira, J. Bernard, Special quasirandom structures, Phys. Rev. Lett. 65 (1990).
[28] A.V. de Walle, T. P, J.M. de, O.D. L, A. M, D. A, S. D, W. Y, C. L, L. Z, C. M, Efficient stochastic generation of special quasirandom structures, Calphad - Comput. Coupling Phase Diagr. Thermochem. 42 (2013) 13–18.
[29] A. van de Walle, M. Asta, G. Ceder, The alloy theoretic automated toolkit: A user guide, Calphad. 26 (2002) 539–553. https://doi.org/10.1016/S0364-5916(02)80006-2.
[30] P. Paufler, J. F. Nye. Physical Properties of Crystals. Clarendon Press — Oxford. First published in paperback with corrections and new material 1985. XVII + 329 p. £ 15.00. ISBN 0-19-851165-5, Cryst. Res. Technol. 21 (1986) 1508–1508. https://doi.org/10.1002/crat.2170211204.
[31] J. Wróbel, L.G. Hector, W. Wolf, S.L. Shang, Z.K. Liu, K.J. Kurzydłowski, Thermodynamic and mechanical properties of lanthanum–magnesium phases from density functional theory, J. Alloys Compd. 512 (2012) 296–310. https://doi.org/10.1016/j.jallcom.2011.09.085.
[32] L.A. Dominguez, R. Goodall, I. Todd, Prediction and validation of quaternary high entropy alloys using statistical approaches, Mater. Sci. Technol. 31 (2015) 1201–1206. https://doi.org/10.1179/1743284715Y.0000000019.
[33] Z. Leong, Y. Huang, R. Goodall, I. Todd, Electronegativity and enthalpy of mixing biplots for High Entropy Alloy solid solution prediction, Mater. Chem. Phys. (2017). https://doi.org/10.1016/j.matchemphys.2017.09.001.
[34] S. Guo, N. C, L. J, L.C. T, Effect of valence electron concentration on stability of fcc or bcc phase in high entropy alloys, J. Appl. Phys. 109 (2011) 10.
[35] Z. Leong, J.S. Wróbel, S.L. Dudarev, R. Goodall, I. Todd, D. Nguyen-Manh, The Effect of Electronic Structure on the Phases Present in High Entropy Alloys, Sci. Rep. 7 (2017) 39803. https://doi.org/10.1038/srep39803.

[36] P.S. Branicio, J.Y. Zhang, D.J. Srolovitz, Effect of strain on the stacking fault energy of copper: A first-principles study, Phys. Rev. B. 88 (2013). https://doi.org/10.1103/PhysRevB.88.064104.

[37] M.S. Lucas, L. Mauger, J. Munoz, Y. Xiao, A.O. Sheets, S.L. Sematin, Magnetic and vibrational properties of high-entropy alloys, J. Appl. Phys. 109 (2011) 7.

[38] M.-H. Tsai, K.-Y. Tsai, C.-W. Tsai, C. Lee, C.-C. Juan, J.-W. Yeh, Criterion for Sigma Phase Formation in Cr- and V-Containing High-Entropy Alloys, Mater. Res. Lett. 1 (2013) 207–212. https://doi.org/10.1080/21663831.2013.831382.

[39] J. Cornide, U. Dahlborg, Z. Leong, L.A. Dominguez, J. Juraszek, S. Jouen, T. Hansen, R. Wunderlich, S. Chambreland, I. Todd, R. Goodall, M. Calvo-Dahlborg, Structure and Properties of Some CoCrFeNi-Based High Entropy Alloys, in: TMS2015 Supplemental Proceedings, 2015.

[40] G.A. Salishchev, M.A. Tikhonovsky, D.G. Shaysultanov, N.D. Stepanov, A.V. Kuznetsov, I.V. Kolodiy, A.S. Tortika, O.N. Senkov, Effect of Mn and V on structure and mechanical properties of high-entropy alloys based on CoCrFeNi system, J. Alloys Compd. 591 (2014) 11–21. https://doi.org/10.1016/j.jallcom.2013.12.210.

[41] H.P. Chou, Y.S. Chang, S.K. Chen, J.W. Yeh, Microstructure, thermophysical and electrical properties in Al x CoCrFeNi (0 ≤ x ≤2) high-entropy alloys, Mater. Sci. Eng. B. 163 (2009) 184–189.

[42] S. Liu, M.C. Gao, P.K. Liaw, Y. Zhang, Microstructures and mechanical properties of Al x CrFeNiTi 0.25 alloys, J. Alloys Compd. 619 (2015) 610–615. https://doi.org/10.1016/j.jallcom.2014.09.073.

[43] M.-R. Chen, S.-J. Lin, J.-W. Yeh, M.-H. Chuang, S.-K. Chen, Y.-S. Huang, Effect of vanadium addition on the microstructure, hardness, and wear resistance of Al0.5CoCrCuFeNi high-entropy alloy, Metall. Mater. Trans. A. 37 (2006) 1363–1369. https://doi.org/10.1007/s11661-006-0081-3.

[44] Z. Leong, I. Todd, R. Goodall, Structural dependency of some multiple principal component alloys with the Thomas-Fermi-Dirac electron density, Scr. Mater. 146 (2018) 95–99. https://doi.org/10.1016/j.scriptamat.2017.11.002.

[45] J.M. Park, T.E. Kim, S.W. Sohn, D.H. Kim, K.B. Kim, W.T. Kim, J. Eckert, High strength Ni–Zr binary ultrafine eutectic-dendrite composite with large plastic deformability, Appl. Phys. Lett. 93 (2008) 031913. https://doi.org/10.1063/1.2952755.

[46] M.G. Poletti, L. Battezzati, Electronic and thermodynamic criteria for the occurrence of high entropy alloys in metallic systems, Acta Mater. 75 (2014) 297–306. https://doi.org/10.1016/j.actamat.2014.04.033.

[47] Y.K. Kim, B.J. Lee, S.-K. Hong, S.I. Hong, Strengthening and fracture of deformation-processed dual fcc-phase CoCrFeCuNi and CoCrFeCu1.71Ni high entropy alloys, Mater. Sci. Eng. A. 781 (2020) 139241. https://doi.org/10.1016/j.msea.2020.139241.

[48] Z. Wu, C.M. Parish, H. Bei, Nano-twin mediated plasticity in carbon-containing FeNiCoCrMn high entropy alloys, J. Alloys Compd. 647 (2015) 815–822. https://doi.org/10.1016/j.jallcom.2015.05.224.

[49] A. Chapuis, Q. Liu, Modeling strain rate sensitivity and high temperature deformation of Mg-3Al-1Zn alloy, J. Magnes. Alloys. 7 (2019) 433–443. https://doi.org/10.1016/j.jma.2019.04.004.

[50] S.L. Shang, A. Saengdeejing, Z.G. Mei, D.E. Kim, H. Zhang, S. Ganeshan, Y. Wang, Z.K. Liu, First-principles calculations of pure elements: Equations of state and elastic stiffness constants, Comput. Mater. Sci. 48 (2010) 813–826. https://doi.org/10.1016/j.commatsci.2010.03.041.

[51] R.S. Mulliken, A New Electroaffinity Scale; Together with Data on Valence States and on Valence Ionization Potentials and Electron Affinities, J. Chem. Phys. 2 (1934) 782. https://doi.org/10.1063/1.1749394.

[52] A. Takeuchi, A. Inoue, Classification of Bulk Metallic Glasses by Atomic Size Difference, Heat of Mixing and Period of Constituent Elements and Its Application to Characterization of the Main Alloying Element, Mater. Trans. 46 (2005) 2817–2829. https://doi.org/10.2320/matertrans.46.2817.

[53] A. Takeuchi, A. Inoue, Mixing enthalpy of liquid phase calculated by miedema's scheme and approximated with sub-regular solution model for assessing forming ability of amorphous and glassy alloys, Intermetallics. 18 (2010) 1779–1789. https://doi.org/10.1016/j.intermet.2010.06.003.

[54] F. Kormann, D. Ma, D.D. Belyea, M.S. Lucas, C.W. Miller, B. Grabowski, H.F. Sluiter, "Treasure maps" for magnetic high-entropy-alloys from theory and experiment, Appl. Phys. Lett. 107 (2015).

[55] U. Dahlborg, J. Cornide, M. Calvo-Dahlborg, T.C. Hansen, A. Fitch, Z. Leong, S. Chambreland, R. Goodall, Structure of some CoCrFeNi and CoCrFeNiPd multicomponent HEA alloys by diffraction techniques, J. Alloys Compd. 681 (2016) 330–341. https://doi.org/10.1016/j.jallcom.2016.04.248.

[56] J. Cornide, M. Calvo-Dahlborg, S. Chambreland, L.A. Dominguez, Z. Leong, U. Dahlborg, A. Cunliffe, R. Goodall, I. Todd, Combined atom probe tomography and TEM investigations of CoCrFeNi, CoCrFeNi-Pdx (x=0.5, 1.0, 1.5) And CoCrFeNi-Sn, Acta Phys. Pol. A. 128 (2015).

[57] W.R. Wang, W.L. Wang, S.C. Wang, Y.C. Tsai, C.H. Lai, J.W. Yeh, Effects of Al addition on the microstructure and mechanical property of AlxCoCrFeNi high-entropy alloys, Intermetallics. 26 (2012) 44–51.

[58] M.-H. Tsai, J.-W. Yeh, High-Entropy Alloys: A Critical Review, Mater. Res. Lett. 2 (2014) 107–123. https://doi.org/10.1080/21663831.2014.912690.

[59] U. Dahlborg, J. Cornide, M. Calvo-Dahlborg, T.C. Hansen, Z. Leong, L.A. Dominguez, S. Chambreland, A. Cunliffe, R. Goodall, I. Todd, Crystalline structures of some high entropy alloys obtained by neutron and x-ray diffraction, Acta Phys. Pol. A. 128 (2015).

[60] M.E. Eberhart, The metallic bond: Elastic properties, Acta Mater. 44 (1996) 2495–2504. https://doi.org/10.1016/1359-6454(95)00347-9.

[61] G. Hua, D. Li, Generic relation between the electron work function and Young's modulus of metals, Appl. Phys. Lett. 99 (2011) 041907. https://doi.org/10.1063/1.3614475.

[62] D.G. Pettifor, Theory of the Heats of Formation of Transition-Metal Alloys, Phys. Rev. Lett. 42 (1978) 846.